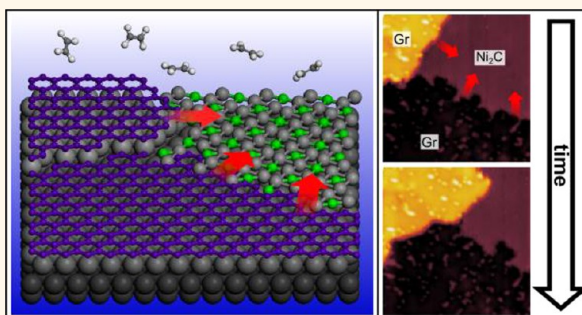


In Situ Observations of the Atomistic Mechanisms of Ni Catalyzed Low Temperature Graphene Growth

Laerte L. Patera,^{†,‡} Cristina Africh,^{†,*} Robert S. Weatherup,[§] Raoul Blume,[⊥] Sunil Bhardwaj,^{||} Carla Castellarin-Cudia,[†] Axel Knop-Gericke,[#] Robert Schloegl,[#] Giovanni Comelli,^{†,‡} Stephan Hofmann,^{§,*} and Cinzia Cepek[†]

[†]CNR-IOM, Laboratorio TASC, Strada Statale 14, Km.163.5, I-34149 Trieste, Italy, [‡]Physics Department and CENMAT, University of Trieste, via A. Valerio 2, I-34127 Trieste, Italy, [§]Department of Engineering, University of Cambridge, Cambridge CB3 0FA, United Kingdom, [⊥]Helmholtz-Zentrum Berlin fuer Materialien und Energie GmbH, Division Solar Energy Research, Berlin 12489, Germany, ^{||}Eletra—Sincrotrone S.C.p.A., Strada Statale 14, Km 163.5, I-34149 Trieste, Italy, and [#]Fritz Haber Institute, D-14195 Berlin-Dahlem, Germany

ABSTRACT The key atomistic mechanisms of graphene formation on Ni for technologically relevant hydrocarbon exposures below 600 °C are directly revealed *via* complementary *in situ* scanning tunneling microscopy and X-ray photoelectron spectroscopy. For clean Ni(111) below 500 °C, two different surface carbide (Ni₃C) conversion mechanisms are dominant which both yield epitaxial graphene, whereas above 500 °C, graphene predominantly grows directly on Ni(111) *via* replacement mechanisms leading to embedded epitaxial and/or rotated graphene domains. Upon cooling, additional carbon structures form exclusively underneath rotated graphene domains.



The dominant graphene growth mechanism also critically depends on the near-surface carbon concentration and hence is intimately linked to the full history of the catalyst and all possible sources of contamination. The detailed XPS fingerprinting of these processes allows a direct link to high pressure XPS measurements of a wide range of growth conditions, including polycrystalline Ni catalysts and recipes commonly used in industrial reactors for graphene and carbon nanotube CVD. This enables an unambiguous and consistent interpretation of prior literature and an assessment of how the quality/structure of as-grown carbon nanostructures relates to the growth modes.

KEYWORDS: graphene · chemical vapor deposition (CVD) · Ni · surface carbide · scanning tunneling microscopy (STM) · X-ray photoelectron spectroscopy (XPS)

The route toward the commercial exploitation of graphene's unique properties hinges entirely on the development of adequate graphene growth and integration technology.¹ Chemical vapor deposition (CVD) is widely seen as the most versatile and promising technique for this. Despite recent progress in achieving graphene CVD over large areas,^{2,3} the growth process and underlying mechanisms have yet to be fully understood. This limits further process and material optimization, and key open questions regarding industrial materials development remain to be addressed. The formation of high quality graphene at reasonably low temperatures largely relies on the use of a catalyst. Ni is a common catalyst choice, both for graphene and carbon nanotube (CNT) CVD,^{4–7} due to the ease of dehydrogenation of

typical hydrocarbon precursors on its surface, followed by the effective formation of a graphitic lattice. In particular, the atomic structure of monolayer graphene (MLG) on Ni(111) is thereby a widely studied model system, based on the close lattice match and related promise for commensurate epitaxial growth of structurally homogeneous graphene.^{8–10} The relatively high carbon solubility of Ni and resulting carbon dissolution and bulk reservoir effect, combined with the vast parameter space of catalytic CVD and the related importance of growth kinetics,^{11,12} however, make growth control and the unambiguous identification of the key growth mechanisms challenging.¹³ Graphene uniformity and layer control over large areas remain very difficult to achieve on Ni. Additional

* Address correspondence to africh@iom.cnr.it, sh315@cam.ac.uk.

Received for review June 10, 2013 and accepted August 7, 2013.

Published online August 08, 2013 10.1021/nn402927q

© 2013 American Chemical Society

complexity arises from reconstructions that Ni surfaces may undergo upon carbon adsorption, e.g., Ni(111) showing a Ni₂C surface phase.¹⁴ Recent literature shows a coexistence of graphene and Ni₂C on Ni(111) and suggests that graphene growth below 460 °C occurs *via* an in-plane conversion mechanism,¹⁵ in contrast to graphene growth *via* carbon attachment directly on Ni(111).^{16–18} This in-plane conversion has been suggested to impose a 3° rotation between the graphene and underlying Ni(111).¹⁵ Rotated MLG on Ni(111), which is unexpected given the widely reported 1 × 1 epitaxial match, has also been linked to graphene growth on top of residual Ni₂C domains¹⁹ or reported to nucleate directly above a critical growth temperature of 650 °C.²⁰ Notably, most data and literature to date is limited by characterization at a postgrowth stage. Hence, despite the atomic structure of graphene on Ni having been investigated for decades, there remains limited direct evidence of the atomistic details involved in the growth process.

Here, we directly study the atomistic mechanisms of graphene formation on Ni *via* complementary scanning tunneling microscopy (STM) and X-ray photoelectron spectroscopy (XPS), both performed *in situ* under *in operando* conditions and supported by systematic *ex situ* CVD calibrations. We focus on technologically relevant hydrocarbon exposures below 600 °C for which our STM data shows a range of coexisting, competing atomic-scale growth mechanisms even for a supposedly simple Ni(111) model surface. We report detailed XPS fingerprints representative of these processes, which allow a direct link to high pressure XPS measurements of a wide range of growth conditions, including polycrystalline Ni catalysts and recipes commonly used in industrial reactors for graphene and CNT CVD.^{5,21,22} Our intention is thereby to capture the entire complexity of the CVD process in order to enable an unambiguous and consistent interpretation of prior literature from different scientific communities and an assessment of how the quality/structure of as-grown carbon nanostructures relates to the growth modes. We find that the relative balance among the atomistic processes, *i.e.*, the dominant graphene growth mechanism, thereby depends not only on conventional CVD parameters such as temperature and pressure but also on the full-history dependent/adventitious near-surface level of carbon in Ni, similar to recent reports for other catalyst metals and CNT growth.^{23,24}

Our *in situ* data shows that a clean Ni(111) surface exposed below 500 °C predominantly shows an initial Ni₂C reconstruction, which converts into MLG either *via* an in-plane mechanism, similar to what has been previously proposed,¹⁵ or *via* a novel two-layer mechanism. We show that the carbide conversion mechanisms thereby always result in epitaxial MLG, *i.e.*, Ni₂C is not a source of graphene grain rotation. Above 500 °C, graphene dominantly grows directly on

clean Ni(111) *via* replacement of Ni surface atoms, which leads to embedded epitaxial and/or rotated MLG domains. Again, we observe no abrupt transition between mechanisms, *i.e.*, no critical transition temperature, rather the relative abundance of rotated MLG domains increases with temperature, indicative of a kinetic selection process. In contrast, given a carbon “contaminated” Ni subsurface prior to the hydrocarbon exposure, we observe no Ni₂C reconstruction even for the lower temperature range, but observe for instance that epitaxial MLG growth directly on Ni *via* the expansion of graphene seeds can predominate across the whole temperature range. Across all experiments, graphene growth occurs during exposure (or on annealing) at fixed temperatures. Carbon precipitation upon cooling is minor, consistent with our previously reported kinetic model¹¹ and the low temperature conditions, but it is noteworthy that if it does occur it is observed exclusively underneath rotated MLG domains, resulting in the formation of Ni₂C. This consistently resolves ambiguity in previous postgrowth data interpretation¹⁹ and agrees well with reported bilayer graphene formation under rotated MLG upon cooling from 650 °C.²⁰ We discuss how our high pressure XPS data allows us to generalize these findings to realistic, scalable graphene growth processes while also being of relevance to the CVD of CNTs and other nanocarbons.

RESULTS AND DISCUSSION

As a representative model system, we focus initially on graphene growth on Ni(111) in the 400–600 °C temperature range and adopt a simple one-step CVD process, whereby the sample is heated and cooled in vacuum, and exposed to an undiluted hydrocarbon precursor (see Methods). We use different base vacuum conditions, both ultrahigh vacuum (UHV, *i.e.*, base pressure <10^{−9} mbar), and high vacuum (base pressure: 10^{−8} to 10^{−6} mbar), to bridge a range of CVD conditions. To take into account the exposure history and carbon contamination level in the Ni layers closest to the surface, we differentiate between clean and carbon-contaminated Ni subsurfaces. The Ni(111) substrates we refer to as having a “clean subsurface” are prepared by multiple cleaning cycles (see Methods) after which no carbon signatures are observed during extended UHV annealing (~30 min in $p < 2 \times 10^{-10}$ mbar) at the growth temperature in both STM and photoemission experiments. The substrates referred to as having a “carbon contaminated subsurface” are samples that even after cleaning show carbon surface signatures (prior to any hydrocarbon exposure) upon heating to the growth temperature. All STM experiments have been repeated several times on different regions of the sample using the same growth conditions to ensure the observed processes are statistically representative. Specifically, we performed about 20 experiments at 410 °C < T < 440 °C, 20 experiments

at $500\text{ }^\circ\text{C} < T < 530\text{ }^\circ\text{C}$, and 5 experiments at $550\text{ }^\circ\text{C} < T < 600\text{ }^\circ\text{C}$, for both clean and carbon contaminated Ni subsurfaces. In the following we focus on the key growth mechanisms for the given conditions, and show representative sequences of STM images in each case. We emphasize though that all the revealed atom-scale mechanisms occur simultaneously, and that it is their relative balance that changes with conditions.

Clean subsurface: Growth at 400–500 °C. Figure 1 shows *in situ* STM images of the Ni catalyst surface during C_2H_4 exposure at $420\text{ }^\circ\text{C}$, representative of different stages of graphene formation during the exposure phase. Figure 1a shows a step edge on the initially clean Ni(111) surface which appears fuzzy due to the fast dynamics of attaching/detaching metal atoms at elevated temperature. We cannot directly resolve Ni mass transport on the terraces, as it occurs on a time scale too short to be followed with our STM scan speed (which requires adatom residence times in surface sites to be $>10^{-4}\text{ s}$), as typical for self-diffusion processes on metallic surfaces.²⁵ After a few minutes of C_2H_4 exposure, an almost complete layer of Ni_2C forms at the surface (Figure 1b). The structure of surface nickel carbide, with Ni_2C stoichiometry, has been investigated and described in previous literature,^{14,19} and is characterized by a peculiar atomic arrangement and related low-energy electron diffraction (LEED) pattern, which we used as fingerprints to interpret our images. In particular, the adsorption of C atoms on Ni(111) induces a surface stress, which is relaxed by a displacement of Ni atoms and by a removal of about 13 atom % of the first metal layer.¹⁴ The Ni and C atoms thereby rearrange into a $\sqrt{39}R16.1^\circ \times \sqrt{39}R16.1^\circ$ overstructure, with an almost square $\sim 5 \times 5\text{ \AA}^2$ cell. In this structure, the Ni surface undergoes a “clock” reconstruction, which is reached by squares of Ni atoms rotating clock- and anticlockwise. This ordered surface carbide (Ni_2C) can be easily recognized in STM by a superstructure characterized by stripes with a periodicity of $\sim 16.5\text{ \AA}$.^{14,19} Indeed, our STM images of the intermediate structure that forms before graphene upon hydrocarbon exposure, shown in Figure 1b, exhibit both stripe periodicity and atomic scale arrangement in perfect agreement with refs 14 and 19 as well as the same LEED pattern, which confirms our assignment.

After several minutes of further continuous exposure, the Ni_2C starts to convert into MLG (Figure 1c), a process which proceeds over a time scale of a few hours at the given conditions, until a complete graphene monolayer is produced (Figure 1d). The atomic scale structure of this graphene layer (see inset Figure 1d) is an ordered honeycomb lattice of C atoms with two inequivalent adsorption sites, separated by a distance equal to the lattice constant of graphene. As previously shown for both experimental and simulated images,^{26–28} the inequivalent adsorption sites of the MLG C atoms, strongly interacting with the Ni

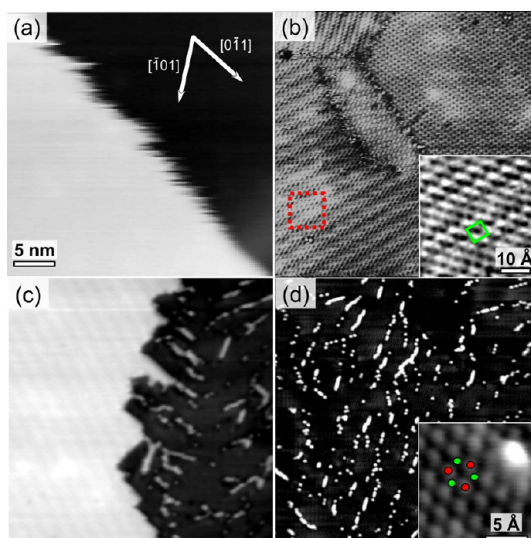


Figure 1. STM images acquired at $420\text{ }^\circ\text{C}$ at different growth stages upon C_2H_4 exposure of clean Ni(111): (a) clean Ni(111) step edge; (b) nickel carbide (Ni_2C) domains on Ni(111). Inset: atomic resolution image of the area in the dotted square. The almost square $5 \times 5\text{ \AA}^2$ unit cell is marked in green. (c) Domain boundary between Ni_2C (left) and graphene (right), during conversion; (d) defected graphene on Ni(111). Inset: Atomically resolved image of graphene. The inequivalent C atoms of a graphene ring are marked in blue and green. The orientation of the crystallographic directions of our sample were identified in atomic resolution images of the clean Ni(111) surface acquired at room temperature (RT) (not shown), and were kept constant in all experiments since the crystal has never been removed nor rotated on the sample holder. Scanning parameters: (a) $V_b = -2\text{ V}$, $I_t = 0.5\text{ nA}$; (b) $V_b = -10\text{ mV}$, $I_t = 1\text{ nA}$; (c) $V_b = -100\text{ mV}$, $I_t = 0.1\text{ nA}$; (d) $V_b = -50\text{ mV}$, $I_t = 0.7\text{ nA}$ (insets: $V_b = -10\text{ mV}$, $I_t = 1\text{ nA}$ (b); $V_b = -300\text{ mV}$, $I_t = 0.5\text{ nA}$ (d)).

substrate, appear as a triangular close-packed array instead of a honeycomb network. The enlargement of such triangular close-packed areas in our STM movies upon further hydrocarbon exposure corroborates their interpretation as MLG. Again, our assignment is consistently confirmed by LEED and XPS (Figure 3), as well as by ultraviolet photoelectron spectroscopy (UPS - see Supporting Information). The lack of a moiré pattern indicates that (i) the mismatch between the Ni(111) substrate and the graphene overlayer is minimal, as expected based on their very close lattice match ($\sim 1\%$),²⁹ and (ii) that the MLG is not rotated relative to the Ni(111) surface. The absence of a rotation angle is also confirmed by the LEED pattern of the final surface (see below). The as-formed graphene is thus epitaxial. We estimate a defect density of $\sim 1\text{--}2\%$, calculated as the fraction of missing C atoms at the bright spots in the STM images, which we suggest are due to the presence of substitutional Ni atoms.

We find the Ni_2C conversion to be the principal graphene growth route on clean Ni for the low temperature range probed ($400\text{--}500\text{ }^\circ\text{C}$). Figure 2 is representative of the behavior observed across our

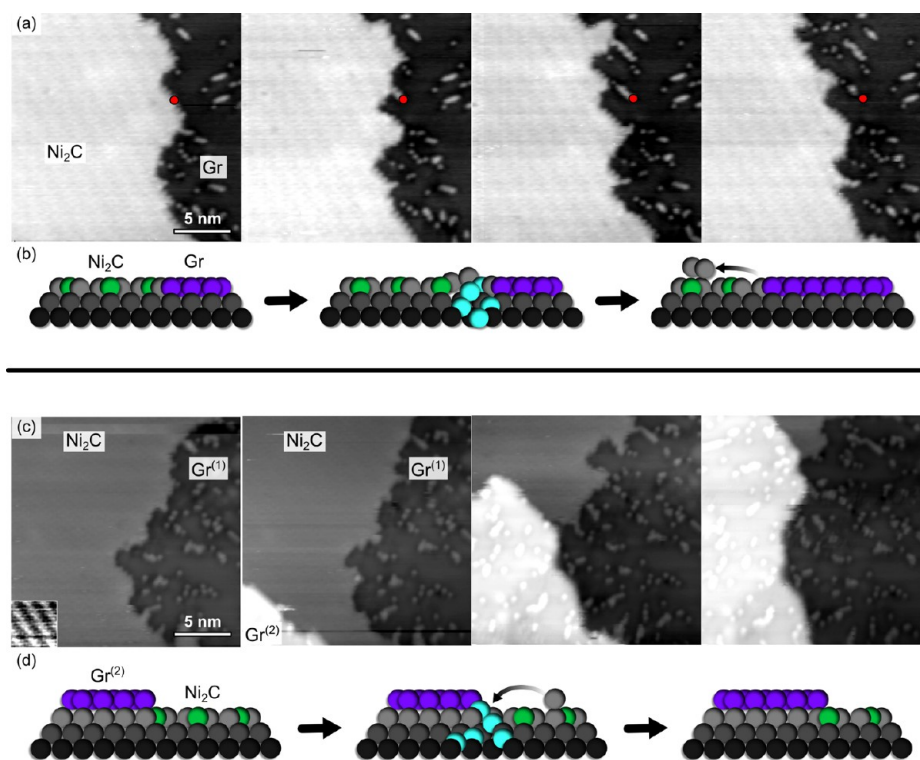


Figure 2. STM images and schematic models of Nickel carbide to graphene conversion: (a and b) in-plane conversion (see corresponding Supplementary Movie S1). In the STM images, the region on the left is covered by Ni_2C , the region on the right by graphene. The red dot marks the position of a fixed defect on the surface. Ni atoms are ejected when additional C atoms reach the surface from the bulk to extend the graphene region. (c and d) Two-layer conversion (see corresponding Supplementary Movie S2). In the STM images, while the graphene region labeled $\text{Gr}^{(1)}$ grows from Ni_2C via in-plane conversion, the graphene island labeled $\text{Gr}^{(2)}$ grows on the same carbide domain by a two-layer conversion mechanism. Here additional C atoms reach the graphene/carbide interface, the Ni layer deconstructs to (1×1) , and the graphene island expands. In the lower left corner of the first STM image in sequence, Ni_2C stripes are highlighted by a different image contrast. In both (a) and (c): $T = 420^\circ\text{C}$, $p(\text{C}_2\text{H}_4) = 2 \times 10^{-7}$ mbar. Time between displayed frames: ~ 120 s (a) and ~ 90 s (c). Scanning parameters: (a) $+V_b = -100$ mV, $I_t = 0.1$ nA; (c) $V_b = -250$ mV, $I_t = 0.5$ nA. In the schematic models, gray/light-blue/green/purple balls represent Ni/dissolved C/carbide C/graphenic C atoms.

experiments, and identifies two different mechanisms by which this conversion proceeds (see corresponding movies in Supporting Information): an in-plane conversion mechanism and a distinct two-layer mechanism. Figure 2a shows STM data representative of the in-plane conversion mechanism. The sequence of images shows a fixed area of the surface scanned at a frame rate of ~ 2 images/min during C_2H_4 (2×10^{-7} mbar) exposure at 420°C . It is clearly seen that the MLG (right-hand side, Figure 2a) expands at the expense of the initial Ni_2C structure (on the left, Figure 2a), whereby the MLG is adsorbed on the same Ni layer supporting the Ni_2C (see Supporting Information for detailed STM analysis). Figure 2b schematically highlights the details of this in-plane conversion mechanism: Ni atoms are ejected from the reconstructed Ni_2C layer and quickly diffuse away due to their high mobility; concurrently, the surface carbon coverage increases and a hexagonal graphitic network forms. As discussed in the following, based on previous literature and supported by our findings on contaminated substrates (see below), we propose that the additional carbon atoms, in this case, reach the carbide/graphene interface from below

the surface and thereby displace and eject Ni surface atoms.

The MLG growth occurs during exposure at fixed temperature, *i.e.*, the widely held assumption that graphene growth on Ni is solely based on carbon precipitation upon cooling^{6,7} is incorrect. During exposure, hydrocarbon molecules adsorb on the Ni surface, dissociate, and C atoms dissolve into the Ni. Ni_2C nucleation and conversion requires the build-up of a sufficient carbon concentration at the Ni surface, which relates to the observed incubation times. In our previous work,¹¹ we established a kinetic model whereby graphene growth proceeds by the build-up of a local carbon supersaturation at the Ni surface, which depends on the flux balance between carbon reaching and leaving the catalyst surface. Carbon can arrive *via* the gas phase (on the clean portion of the surface or through defects on already carbon-covered areas) or *via* segregation from the catalyst bulk, while it can leave *via* diffusion into the catalyst bulk. This general kinetic model is applicable to every kind of substrate, both for the Ni_2C formation and conversion, as well as for graphene formation directly on Ni. It is interesting

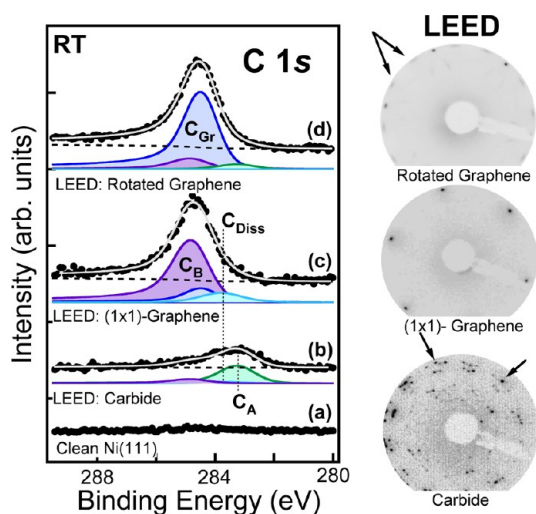


Figure 3. C 1s XPS spectra (left), and corresponding negative of the LEED patterns (right) of (a) clean Ni(111), (b) carbide, (c) epitaxial graphene, (d) rotated graphene phases. The photoemission spectra are acquired at RT in normal emission geometry using a conventional Mg K α X-ray source at an overall energy resolution of ~ 0.8 eV. Superimposed to the C 1s experimental data (dots) are the fitting results (light gray) together with the Shirley background (dotted line) and the four Doniach-Šunjić C_A (green), C_B (purple), C_{Gr} (blue) and C_{Diss} (light-blue) components (see text for further details). All LEED are acquired at RT (E_p : ~ 70 eV). The arrows in the carbide LEED image indicate the position of two (1 \times 1) spots, while the arrows in the rotated graphene LEED image indicate the extra spots of the moiré pattern.

to note that in model systems the Ni₂C layer has been reported to passivate the Ni catalyst surface (at least at step edges).³⁰ This can impede carbon precursor dissociation in an analogous manner to graphene coverage.¹¹ The more complete this passivation, the more the carbon flux to the Ni surface/interface will be dominated by isothermal segregation from the Ni bulk. This may account for the notable delay we observe in graphene nucleation following Ni₂C formation.

The general scenario of carbon dissolution and re-segregation to the surface to form graphene by the observed in-plane Ni₂C conversion mechanism is similar to what has been proposed by Lahiri *et al.*,¹⁵ and is also consistent with their DFT results, showing that the process in which Ni atoms at the carbide/graphene interface are removed from Ni₂C and replaced by carbon atoms from the bulk is exothermic.¹⁵ This previous postgrowth data, however, showed a 3° rotation between the graphene and underlying Ni(111), which was suggested to be due to the preference of the growing graphene to form a coincidence structure with the surface carbide at their 1D interface.¹⁵ Our *in situ* data clearly shows that in all cases Ni₂C conversion leads to only epitaxial graphene formation and we further show that inconsistencies in literature regarding the formation of rotated domains due to Ni₂C are likely to arise from ambiguity in the interpretation of postgrowth data^{15,19} as discussed in detail below.

Figure 2c shows STM data representative of a different, two-layer Ni₂C conversion mechanism (see Supporting Information for full STM movie). While the graphene island labeled Gr⁽¹⁾ grows *via* the in-plane conversion mechanism described above at the edges of the Ni₂C region, the MLG domain labeled Gr⁽²⁾ appears to expand *on* (and exclusively *on*) the same Ni₂C region. Our height analysis in the Supporting Information clearly shows that Gr⁽²⁾ grows *on* a metal atomic layer, probably formed from Ni atoms which were initially part of the Ni₂C along with additional Ni atoms fast diffusing on the surface (see Supporting Information), rather than as an overlayer on the Ni₂C as previously suggested,¹⁹ or as a bilayer graphene region. This last statement is also confirmed by *ex situ* photoemission results, which only indicate the presence of epitaxial MLG for the same final surface. The proposed conversion process leading to the formation of the Gr⁽²⁾ graphene domain is schematically outlined in Figure 2d: carbon atoms in the Ni₂C layer are promoted one layer higher, while the Ni surface deconstructs back to (1 \times 1), requiring mass transport to supply the additional Ni. Further carbon atoms arrive, and a graphene island forms. The reaction/conversion front of this two-layer mechanism proceeds at ~ 0.8 Å/s, much faster than the reaction front of the in-plane conversion (~ 0.15 Å/s, values extracted from Movie S2). For the in-plane conversion, the topmost Ni atoms corresponding to 87% of a Ni(111) layer have to be locally removed, while for the two-layer conversion, additional Ni atoms corresponding to only 13% of a Ni(111) layer are required to reconstruct the topmost metal layer. We note that the difference in graphene growth rate between the mechanisms may relate to this difference in the required Ni mass transport. In the temperature range considered here, however, we always find the most common growth process to be the in-plane conversion mechanism, indicating a kinetic selection dominated by a lower nucleation barrier for this process. Again, the Ni mass transport involved in both of these Ni₂C conversion mechanisms cannot be resolved with the available STM time resolution. It is important to note, that none of our post-growth measurements reveal the formation of further carbon structures underneath the epitaxial MLG on Ni(111) following cooling.

Chemical Identification of the C Species. We further investigate the carbide conversion mechanisms using complementary *in situ* and *ex situ* XPS to provide a record and fingerprint of the chemical evolution of the Ni(111) surface during graphene formation over a much larger area (~ 0.01 – 1 mm² spot size range). We focus first on obtaining XPS fingerprints for each of the surface structures observed with STM, by reproducing the same experimental conditions used for STM in a conventional UHV XPS system (see Methods). Figure 3 shows the C 1s core levels (left), and the

corresponding LEED patterns (right) acquired at RT of clean Ni(111) (Figure 3a), Ni₂C (Figure 3b), and graphene covered Ni(111) (Figure 3c,d) surfaces. The LEED provides a direct link with the structures observed in STM, as a morphological check to confirm that the expected phase is produced across the surface. We follow the same deconvolution of the XPS C 1s spectra as in ref 5 using the same four key components, C_A (283.2 eV), C_{Dis} (283.8 eV), C_{Gr} (284.4 eV), and C_B (284.8 eV).

The C 1s spectrum of the graphene covered Ni(111) surface in Figure 3c shows a dominant C_B component, ~72% of the total C 1s intensity, with the C_{Dis} and C_{Gr} contributing ~12% and ~15%, respectively, while the intensity of C_A is negligible (<1%). LEED shows the hexagonal pattern expected for epitaxial graphene on Ni(111), and we thereby assign C_B to epitaxial graphene. We note that the C_B peak position corresponds also to carbon atoms with different bonding configurations,^{31,32} the presence of which can be excluded here based on our STM observations. C_{Dis} has previously been identified as interstitial carbon dissolved in to the Ni forming a Ni-rich solid solution.^{5,33} C_{Gr} has the same energy as for pristine HOPG,³⁴ and is thus assigned to weakly coupled and nondefective graphene layers, which may include rotated graphene, additional graphene layers, or graphene decoupled from the Ni surface *e.g.*, by intercalation of adspecies.³⁵ During STM experiments few rotated graphene islands have been observed, and we thus assign the weak C_{Gr} peak to rotated graphene for the low pressure (<10⁻⁶ mbar) and low temperature (<500 °C) conditions considered here.

For the Ni₂C covered Ni(111) surface (Figure 3b), the most intense peak is C_A (71%), with some C_B (18%, corresponding to a coverage of ~5% of the Ni(111) surface), a small percent of C_{Dis} (~7%), and negligible C_{Gr} (4%) (last two components not visible in figure scale). The presence of Ni₂C on the Ni(111) surface is confirmed by the appearance of its typical LEED pattern³⁶ as shown in Figure 3. Our analysis also indicates that the intensity ratio between the C_B peak of the graphene covered Ni(111) surface and the C_A peak of the Ni₂C covered Ni(111) surface is 4.0:1, which within experimental error corresponds to the ratio of the carbon atomic densities of graphene and Ni₂C (4.7:1).¹⁴ However, we also expect that carbon bonded at Ni surface sites, not necessarily forming a long-range ordered structure, would show a component of similar binding energy resulting from a similar charge transfer from Ni to embedded C atoms. This broader assignment of C_A could account for previous observations of a C_A peak under conditions where Ni₂C may be unstable,^{5,21} and will be addressed in a further publication. Given the direct correspondence between our XPS and STM results, for the conditions used herein on Ni(111)

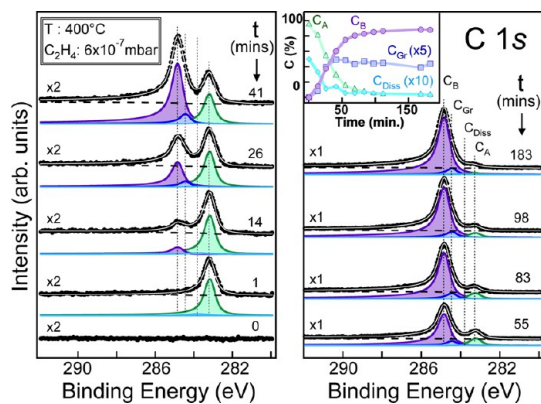


Figure 4. Time-resolved *in situ* high resolution XPS C 1s core level spectra during low pressure CVD on a “clean subsurface” Ni(111) single crystal [base pressure $\sim 10^{-7}$ mbar, $T = 400$ °C, $p(\text{C}_2\text{H}_4) = 6 \times 10^{-7}$ mbar]. Time = 0 is relative to when the C₂H₄ valve is opened and spectral acquisition begins, however exposure pressure is not instantaneously reached. All spectra are collected in normal emission geometry at photon energies of 435 eV (surface sensitive; $\lambda_{\text{escape}} \approx 7$ Å) with a spectral resolution of ~ 0.3 eV. Superimposed to the C 1s experimental data (dots) are the fitting results (light gray) together with the Shirley background (dotted line) and the four Doniach-Sunjić C_A (green), C_B (purple), C_{Gr} (blue) and C_{Dis} (light-blue) components (see text for further details). The inset shows the percentage of the different carbon species (C_A (green triangles), C_B (purple dots), C_{Gr} (blue squares) and C_{Dis} (light-blue diamonds), as determined by the area under the corresponding peaks.

surfaces, we conclude that C_A relates to Ni₂C, while C_B relates to epitaxial graphene.

Figure 4 shows the time-resolved chemical evolution of the C 1s spectra for the Ni(111) surface during graphene growth, measured using synchrotron radiation (see Methods). We observe the appearance of the same four, principal components as identified earlier (C_A, C_{Dis}, C_{Gr} and C_B). On C₂H₄ exposure, C_A and a weak C_{Dis} signal initially appear, followed by the emergence of the C_B and a smaller C_{Gr} component. C_B grows with continuing hydrocarbon exposure becoming the dominant species, accompanied by a strong reduction in the C_A peak intensity, until the C_B peak intensity almost saturates (the exposure was stopped before reaching complete monolayer coverage). C_{Gr} also grows concurrently with C_B but its intensity remains <10% that of the dominant C_B peak. This peak evolution allows us to generalize our findings for a wider range of vacuum conditions (both base and exposure pressures): as soon as the hydrocarbon exposure starts, carbon dissociates on the bare Ni(111) surface, dissolves in to the Ni leading to an increase in the level of dissolved carbon in the subsurface, and the Ni₂C phase forms across the surface. In this case the induction time is shorter than for STM experiments (~ 1 min vs ~ 10 mins), as expected due to the higher C₂H₄ pressure (~ 3 times).¹¹ With continuing hydrocarbon exposure, the Ni₂C gradually transforms into epitaxial graphene until almost complete coverage with an epitaxial graphene monolayer is achieved (see Supporting Information for

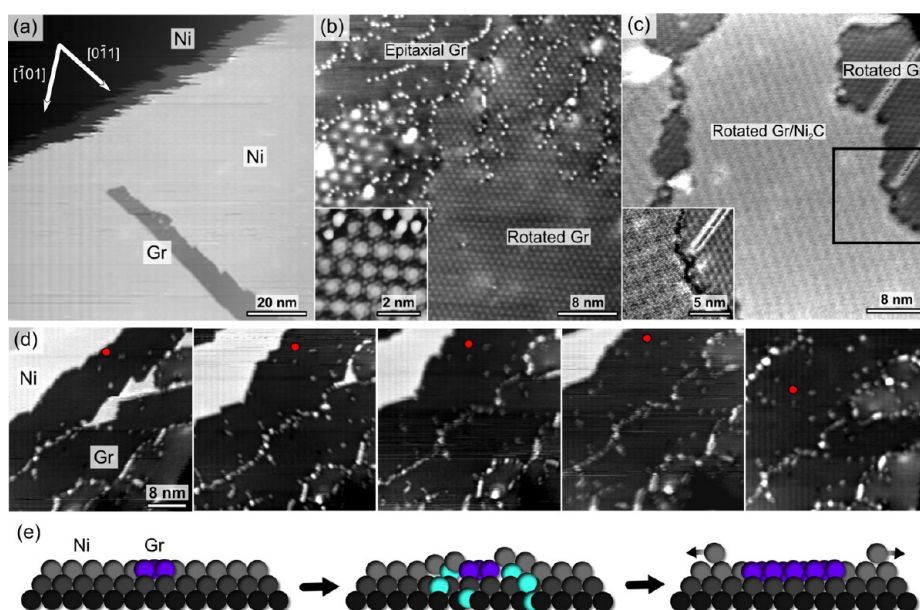


Figure 5. STM images and schematic models of graphene growth on clean Ni(111) above 500 °C. All images acquired at 520 °C unless specified. (a) Embedded graphene island (dark stripe) in the middle of a clean Ni(111) terrace. (b) Final MLG layer after growth, showing regions of rotated (right) and of epitaxial (top-left) graphene [$V_b = -600$ mV, $I_t = 1$ nA]. Inset: atomic resolution image highlighting the moiré pattern on rotated graphene [$V_b = -10$ mV, $I_t = 1$ nA]. (c) STM image at RT showing a graphene covered region grown at 520 °C after cooling at room temperature: Ni₂C islands form below rotated graphene regions [$V_b = -200$ mV, $I_t = 2$ nA]. Inset: magnification of the boundary between rotated graphene (right) and graphene on Ni₂C (left) [$V_b = -100$ mV, $I_t = 2$ nA]. (d and e) Growth mechanism (see corresponding Supplementary Movie S3). Graphene islands embedded into the Ni substrate expand by segregation of additional C atoms and ejection of additional Ni atoms. The red dot marks the position of a fixed defect on the surface. In the schematic models, gray/light-blue/green/blue balls represent Ni/dissolved C/carbidic C/graphenic C atoms. [$p(\text{C}_2\text{H}_4) = 2 \times 10^{-7}$ mbar, consecutive images with acquisition time ~ 30 s/frame. Scanning parameters: $V_b = -2$ V, $I_t = 0.5$ nA.]

details on carbide to graphene conversion growth rate). The presence of the small C_{Gr} peak that accompanies C_B indicates that a small proportion of the surface is covered with rotated graphene. We emphasize that for our previous observations on polycrystalline films, the same four XP components can be consistently fitted and the order of peak appearance remains the same.^{5,21} This is also the case for graphene growth from different carbon sources, including gaseous hydrocarbons (C_2H_2 , C_2H_4 , and C_6H_6), as well as solid carbon sources (tetrahedral amorphous carbon). This highlights that the detailed growth mechanisms observed using STM on Ni(111) surfaces during C_2H_4 exposure are also important for technologically relevant polycrystalline catalysts and a number of different carbon sources, in spite of the added complexities of multiple surface orientations and differences in the carbon supply. Our detailed interpretation of XPS signatures allows us to bridge the so-called pressure and materials gap,³⁷ *i.e.*, to generalize our findings to realistic, scalable graphene growth processes while also being of relevance to the CVD of carbon nanotubes (CNT) and other nanocarbons.

Clean subsurface: Growth at 500–600 °C. Figure 5 shows representative STM images of graphene growth on clean Ni(111) above 500 °C. Ni₂C formation during the first growth stages is progressively reduced, although not completely suppressed, as the exposure temperature is increased above 500 °C, and a different dominant

graphene growth route sets in, as revealed by the STM images, whereby graphene grows directly on Ni(111) *via* Ni replacement mechanisms. After nucleation, graphene islands grow embedded into the Ni surface, preferentially elongated in a close-packed Ni(111) direction (see dark stripe in Figure 5a, and detailed STM height analysis in Supporting Information). The final complete monolayer includes not only epitaxial regions, but also moiré domains, as shown in Figure 5b. The moiré domains are due to a rotation of the graphene layer with respect to the underlying Ni(111) surface (see Supporting Information). The balance between epitaxial and rotated domains in the final MLG surface shows a strong dependence on the growth temperature: at higher temperatures, rotated domains are increasingly present in STM images, and, at the same time, arches of extra spots appear in the LEED pattern, centered at $\sim 20^\circ$, as shown by the arrows in Figure 3. Growth of rotated MLG directly on Ni(111) is consistent with a previous LEED/LEEM study,²⁰ albeit therein a critical growth temperature of 650 °C was assumed. Indeed, DFT studies predict only a small energy difference between stable epitaxial graphene configurations and less interacting configurations with a lack of preferred C–Ni registry.³⁸ We therefore attribute the increasing coverage of rotated graphene for increasing temperature to kinetic effects. We have not captured here the very first nucleation stages, but the sequence

of STM images in Figure 5d (STM movie S3, available in Supporting Information) illustrates how embedded graphene regions grow. Elongated MLG islands expand on the same terrace, one toward the other, at $\sim 1 \text{ \AA/s}$, progressively reducing the width of the bare Ni surface in between, until only a line of point defects remains. This growth mechanism can be rationalized as schematically outlined in Figure 5e: when a first graphene nucleus is present, additional C atoms segregate to the surface at its borders, facilitating the ejection of Ni atoms, and attach to the graphene island edges, thus replacing surface Ni atoms. In this way, the anchoring points are shifted and the MLG island expands. A similar growth by the removal of metal atoms at graphene edges has also been observed on Rh(111)²⁴ and Ru(0001),^{39,40} albeit as a more minor growth mechanism. The dominant growth mechanism for these surfaces is typically carbon attachment to the edges of graphene islands atop the metal. This difference in dominant growth mechanism may relate to the significantly higher carbon solubility of Ni compared to Rh and Ru,^{8,41} which may facilitate Ni atom ejection. It is noteworthy that we have also observed a mechanism here by which MLG islands expand directly atop Ni(111), *i.e.*, where the graphene is not embedded. However, as outlined below, we find this mechanism to be dominant only in the case of a carbon contaminated subsurface. A previous LEEM study,¹⁸ suggested that graphene islands grow by C addition to “free” graphene edges upon prolonged exposure of Ni(111) to ethylene at 550 °C, *i.e.*, comparable conditions to our embedded growth on clean Ni in the 500–600 °C range. This apparent disparity may be associated with the huge mass transport involved in the embedded growth mechanism. This Ni mass transport, which we observe preceding the embedded graphene growth front, may relate to the surface diffusion processes previously suggested based on LEEM measurements.¹⁸ Indeed, when imaging clean Ni terraces by STM during graphene growth, we sometimes observed a sudden change in the morphology, with new Ni layers forming above the previously imaged topmost layer, on which the growth of embedded graphene then proceeds. Notably, for lower growth temperatures, the present STM and previous LEEM investigations agree in the identification of a process that involves carbide conversion.

Upon cooling of the MLG covered surface to room temperature, a different STM contrast appears in some regions (roughly 30–50%) of the rotated graphene (Figure 5c). This different contrast was previously observed, and attributed, based on detailed analysis, to the presence of Ni₂C islands underneath the rotated MLG.¹⁹ Our *in situ* data here clearly shows that this structure results from the precipitation of carbon upon cooling. This agrees well with our *ex situ* XPS data

(Figure 3d), acquired on the same MLG covered surface as imaged with STM, which confirms the presence of both rotated graphene and carbide after cooling to RT. Detailed XPS data analysis shows that the major contribution to the C1s spectrum comes from the C_{Gr} component (surface coverage: $\sim 87\%$), assigned to rotated domains, with a small percentage of epitaxial graphene C_B (surface coverage: $\sim 13\%$), and negligible C_{DIS} ($< 1\%$). Given that our STM results reveal that the carbide is formed upon cooling only below rotated graphene, XPS data analysis (see Supporting Information) suggests $\sim 37\%$ of the rotated graphene has carbide underneath, in agreement with our STM measurements. The observed lower binding energy of the rotated graphene overlayer (C_{Gr}) is almost the same as for weakly interacting graphene layers.^{42,43} This suggests that the bonding with the substrate is characterized by a lower charge transfer from the Ni(111) than in the case of an epitaxial overlayer, due to the lack of a direct Ni-top-C interaction, which is responsible for most of the charge transfer in MLG.⁴⁴ This consistently resolves ambiguity in previous postgrowth data interpretation¹⁹ and agrees well with reported bilayer graphene formation under rotated MLG upon cooling from 650 °C.²⁰

Carbon-Contaminated Subsurface: Growth at 400–600 °C.

The mechanisms established above all refer to conventional CVD parameters such as temperature and pressure, which can be carefully controlled. Figures 6 and 7, however, show that the dominant graphene growth mechanism critically depends also on the near-surface carbon concentration which is much more difficult to control as it is intimately linked to the full history of the catalyst and all possible sources of contamination. We previously highlighted how minor, routinely present levels of carbon contamination can significantly influence CNT growth kinetics.²³ Here we show that the graphene growth scenario can change completely if the Ni(111) substrate does not undergo a complete cleaning procedure and some residual carbon contamination is present in the subsurface, a case which we refer to as “carbon-contaminated subsurface”. For this case, even though the Ni surface appears clean at RT in XPS and LEED, with only some small carbide islands present in STM images, as soon as the temperature is increased to the growth temperature, prior to exposure, we observe the formation of graphene seeds at the Ni surface, both at Ni steps (Figure 6a), and as small islands on top of metal terraces (Figure 6b). Once at the growth temperature, in UHV conditions, the seeds expand even without gas exposure, fed by C atoms from the subsurface reservoir, leading to a complete, mainly epitaxial MLG coverage over the whole temperature range investigated (Figure 6c), without any intermediate carbide phase. This picture is confirmed by all our XPS (Figure 7), STM and LEED (not shown) experiments. The expansion of the graphene seeds thereby occurs

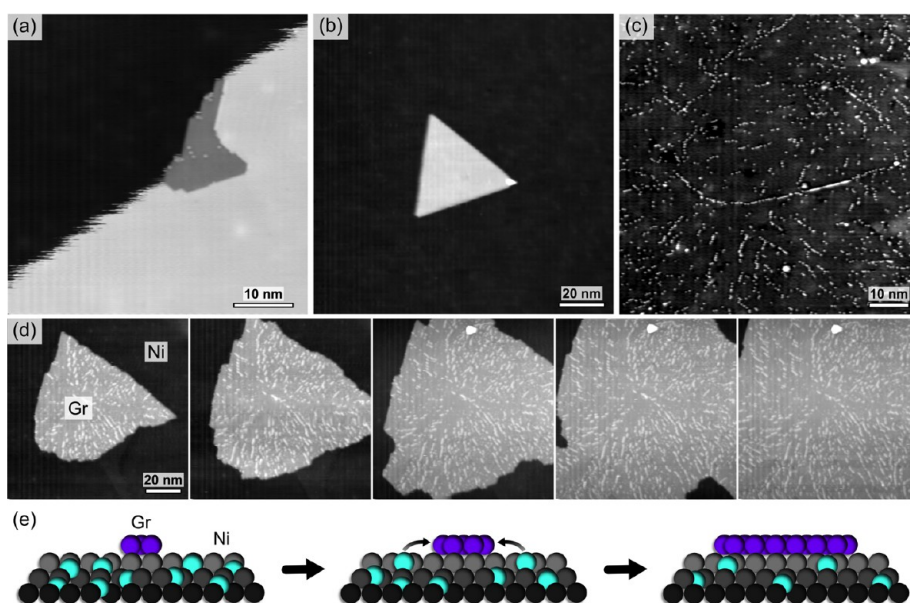


Figure 6. Graphene growth on Ni in case of C-contaminated subsurface. STM images during annealing at 520 °C (a–c). Graphene seeds are already present as soon as the temperature is reached, both at step edge (a) [$V_b = -600$ mV, $I_t = 0.5$ nA] and on a terrace (b) [$V_b = -300$ mV, $I_t = 0.8$ nA]; (c) the complete epitaxial MLG after ~ 1 h [$V_b = -400$ mV, $I_t = 0.7$ nA]. (d) STM images of a graphene seed growth on a Ni terrace at 410 °C without hydrocarbon exposure ($p_{bg} = 2 \times 10^{-10}$ mbar, see corresponding Supplementary Movie S4). The expansion occurs by C attachment to the edges. Time between displayed frames: ~ 10 min. Scanning parameters: $V_b = -600$ mV, $I_t = 0.4$ nA. (e) Schematic model of the growth mechanism imaged in (d), gray/light-blue/purple balls represent Ni/dissolved C/graphenic C atoms.

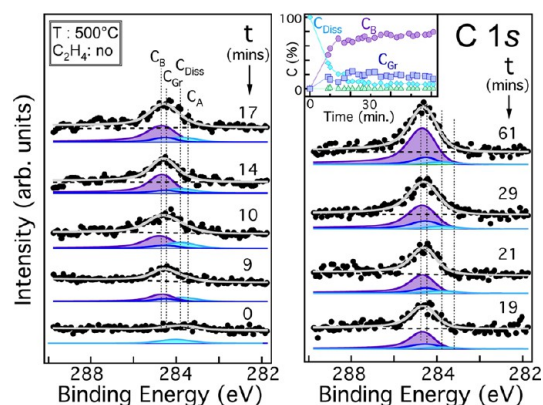


Figure 7. Time-resolved *in situ* low resolution XPS C 1s core level spectra during annealing at 500 °C the “carbon contaminated subsurface” Ni(111) single crystal [pressure during annealing $\sim 10^{-10}$ mbar, $p(C_2H_4) = 0$ mbar]. Time = 0 is relative to when the spectral acquisition begins. All spectra are collected in normal emission geometry at photon energies of 1253.6 eV (surface sensitive; $\lambda_{escape} \approx 15$ Å) with a spectral resolution of ~ 0.8 eV. Superimposed to the C 1s experimental data (dots) are the fitting results (light gray) together with the Shirley background (dotted line) and the four Doniach-Sunjić C_A (green), C_B (purple), C_{Gr} (blue) and C_{Dis} (light-blue) components (see text for further details). The inset shows the percentage of the different carbon species [C_A (green triangles), C_B (purple dots), C_{Gr} (blue squares) and C_{Dis} (light-blue diamonds)], as determined by the area under the corresponding peaks.

on top of the Ni substrate, by C atom addition to graphene edges, as shown by the selected frames in Figure 6d (see corresponding Supplementary Movie S4) and schematically outlined in Figure 6e. Such graphene growth in UHV without hydrocarbon

exposure is clear evidence of the capability of subsurface C to diffuse to the surface and form graphene. This further corroborates the growth models on clean Ni described in the previous sections. Our investigations of seeded graphene growth are ongoing and the related details are beyond the scope of this paper. We find it important here, however, to highlight the significance of developing a strategy to control all growth parameters, in particular the substrate contamination, as it has so far been widely neglected across the literature. We highlight that consideration of the influence of such minor carbon contamination is also highly relevant when comparing UHV data to more realistic CVD conditions used in industrial reactors.

CONCLUSIONS

We have directly revealed and characterized a number of competing atomistic mechanisms of graphene formation on Ni for technologically relevant low temperature CVD *via* complementary STM and XPS, both performed *in situ* under *in operando* conditions and supported by systematic *ex situ* CVD calibrations. Figure 8 schematically summarizes the dominant growth routes with respect to the CVD conditions and the initial level of subsurface carbon. For clean Ni(111), below 500 °C the formation of an intermediate, structural surface carbide (Ni_2C) is favored, which converts into epitaxial graphene. Above 500 °C, graphene predominantly grows directly on Ni(111) *via* replacement mechanisms leading to embedded epitaxial and/or

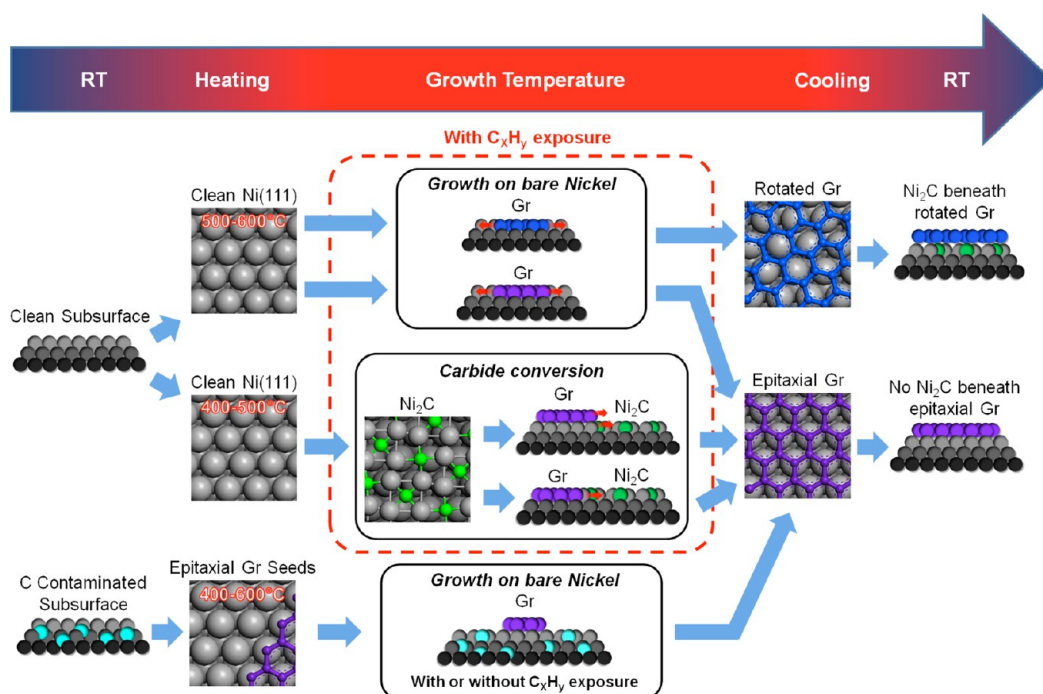


Figure 8. Schematic overview of the different graphene growth routes on Ni(111).

rotated graphene domains. Surface carbide formation is thereby not the source of graphene grain rotation, rather rotated graphene domains nucleate directly on Ni(111) at sufficiently high temperatures and their increased relative abundance (compared to epitaxial domains) with increasing temperature is kinetically determined. We show that the dominant graphene growth mechanism critically depends not only on conventional CVD parameters but also on the near-surface carbon concentration which is much more difficult to control, as it is intimately linked to the full history of the catalyst and all possible sources of contamination. Given a carbon-contaminated surface prior to hydrocarbon exposure, for instance, epitaxial MLG growth directly on Ni *via* the expansion of such seeds by C addition at their edges above the substrate predominates across the whole temperature range probed.

Importantly, in all the explored conditions, graphene grows isothermally up to a complete monolayer. Upon cooling, further changes can occur. In particular, on Ni(111) we observed the formation of Ni₂C regions underneath rotated graphene domains and on bare Ni(111), but not underneath epitaxial graphene. Given that not only Ni₂C but also an additional graphene layer would grow only at the interface between the Ni and the existing graphene layer, *i.e.*, in contact with the Ni, as also observed for CNT growth,^{4,45} this suggests that the strong interaction of epitaxial MLG on Ni(111) significantly increases the energy barrier for further graphene layer nucleation.

Further to the data reported here, our previous high-pressure XPS measurements of growth on polycrystalline

Ni (550 nm films and 25 μm foils),^{5,21} performed across a broad range of hydrocarbon pressures, allow us to generalize our findings. In particular, we have observed a general trend for a reduction in the C_A peak intensity with increasing growth temperature, and a related shift in the C_B to C_{Gr} ratio toward the latter. This is consistent with the shift in the balance of growth mechanisms from graphene growth by transformation of an intermediate surface carbide toward the direct growth of rotated graphene (Figure 8).

As known from literature and our prior work, for higher CVD exposure pressures self-limitation to monolayer graphene coverage can not necessarily be assumed, and particularly for Ni it is very challenging at high pressures to achieve graphene uniformity and layer control.^{6,7,21} Given the possibility of much higher carbon supersaturations at the Ni surface, we suggest based on our data here (Figure 8) that higher precursor exposure pressures favor the nucleation of rotated graphene domains, lowering the nucleation barriers for multilayer graphene by decoupling the graphene from the Ni surface. Indeed, recent postgrowth STM data indicates a prevalence of multilayer graphene consisting of rotated domains during atmospheric pressure CVD on polycrystalline Ni.⁴⁶ A less strongly interacting graphene layer, such as rotated MLG, may also facilitate graphene growth across the grain boundaries of polycrystalline catalysts, as previously shown for polycrystalline Ru.⁴⁷

We believe that the understanding of the atomic scale growth mechanisms established here is highly relevant for the controlled graphene growth over a broad range of conditions and, in particular with

regard to the question of how quality/structure relates to the underlying growth modes, is of general

relevance to all related catalytically grown carbon nanostructures.

METHODS

We performed *in situ* STM under *in operando* conditions to monitor the structural evolution of the (111) surface of a Ni single crystal (~ 1 mm thick) during exposure to C_2H_4 (10^{-7} mbar pressure range) at 400–600 °C. We combine this with both *ex situ* and *in situ* XPS and UPS experiments in a conventional UHV chamber, and with *in situ*, time-resolved XPS measurements with synchrotron radiation on Ni(111) during C_2H_4 (10^{-6} mbar pressure range) exposures. Before exposure, the Ni(111) surface was carefully cleaned, as confirmed by a clear hexagonal LEED pattern and by the absence of any C structure in STM images acquired at RT, and the absence of any C peak in XPS spectra. In all experiments, the sample temperature was measured with a K-type thermocouple spot-welded on the Ni single crystal.

STM experiments have been performed in a UHV (base pressure: $\sim 10^{-10}$ mbar) chamber equipped with standard preparation/characterization facilities (sputter gun, heating stage, gas line, LEED) and a commercial Omicron VT-STM, modified to yield atomic resolution measurements at high temperature up to 600 °C and in reactive environment, with a frame-rate of 1–2 images/min. The Ni(111) sample was cleaned by repeated cycles of Ar^+ sputtering (15 min, 2 KeV) and flash annealing (600 °C) in UHV. The cleaning cycles were stopped when the sample did not show any C structure at RT, such as Ni_2C islands at the step edges, suggesting a very low carbon contamination in the single crystal. Growth studies were performed by back-filling the chamber with C_2H_4 (2×10^{-7} mbar – to be locally corrected for an estimated screening factor of 5 in the area shadowed by the tip⁴⁸) while acquiring a series of consecutive STM images at frame rate of ~ 2 images/min.

The UHV (base pressure: $\sim 10^{-10}$ mbar) *in situ* and *ex situ* photoemission spectra acquired on Ni(111) were measured at RT in normal emission geometry, using a hemispherical electron energy analyzer, and a conventional Mg Ka X-ray source ($h\nu$: 1253.6 eV) and a He lamp ($h\nu$: 40.8 eV). The overall energy resolution for the XPS and UPS spectra were, respectively, ~ 0.8 and ~ 0.2 eV. The XPS binding energies scale was calibrated by setting the Ni $2p_{3/2}$ peak of the clean Ni(111) at 852.6 eV.

In situ, time-resolved high-resolution XPS experiments were performed at the ISSS beamline of the Fritz Haber Institute located at the BESSY II synchrotron facility in Berlin. The high-pressure setup consists mainly of a reaction cell (base pressure $\sim 10^{-7}$ mbar) attached to a set of differentially pumped electrostatic lenses and a differentially pumped analyzer (Phoibos 150, SPECS GmbH), as described elsewhere.⁴⁹ Samples were pretreated by oxidation ($p(O_2) = 1 \times 10^{-4}$ mbar, 30 s) and reduction ($p(H_2) = 1 \times 10^{-4}$ mbar, 3 min) at ~ 600 °C to leave a clean Ni surface with no detectable C species in the C 1s spectra, prior to hydrocarbon exposures. All spectra are collected in normal emission geometry at photon energies of 425 eV (surface sensitive: $\lambda_e \approx 7$ Å, where λ_e is the inelastic mean free path of the photoelectrons at ~ 425 eV kinetic energy in solids), with a spot size of $80 \mu m \times 150 \mu m$. Time signatures are relative to when the C_2H_4 valve is opened and spectral acquisition begins.

All C 1s spectra were analyzed by performing a nonlinear mean square fit of the data, using four Doniach-Sunjić components superimposed on a Shirley background. The asymmetries and Lorentzian linewidths were extracted from the high-resolution spectra, by fixing the asymmetries of the C_{Dis} component to zero, while leaving as free parameters in the fit procedure those of C_A , C_{Gr} and C_B . The resulting asymmetries of the C_{Gr} and C_B components were the same, 0.144, while the C_A asymmetry, determined from the deconvolution of the pure carbide phase, was 0.089. The intrinsic Lorentzian line width G was ~ 0.24 eV, compatible with literature results in carbon-based materials. The low-resolution spectra were analyzed using the so-obtained asymmetries and Lorentzian width values.

Conflict of Interest: The authors declare no competing financial interest.

Acknowledgment. L.L.P. acknowledges funding from Area di Ricerca Scientifica e Tecnologica di Trieste and from MIUR through Progetto Strategico NFFA. C.A. acknowledges support from CNR through the ESF FANAS project NOMCIS. C.A. and C.C. acknowledge financial support from MIUR (PRIN 2010-2011 no. 2010N3T9M4). S.B. acknowledges funding from ICTP TRIL program. S.H. acknowledges funding from ERC grant InsituNA-NO (no. 279342). R.S.W. acknowledges funding from EPSRC (Doctoral training award), and the Nano Science & Technology Doctoral Training Centre Cambridge (NanoDTC). The help of C. Dri and F. Esch (design) and P. Bertoch and F. Salvador (manufacturing) in the realization of the high temperature STM sample holder is gratefully acknowledged. We acknowledge the Helmholtz-Zentrum-Berlin Electron storage ring BESSY II for provision of synchrotron radiation at the ISSS beamline and we thank the BESSY staff for continuous support of our experiments.

Supporting Information Available: STM movie files, detailed STM image analysis and details of XPS analysis. This material is available free of charge via the Internet at <http://pubs.acs.org>.

REFERENCES AND NOTES

- Novoselov, K. S.; Fal'ko, V. I.; Colombo, L.; Gellert, P. R.; Schwab, M. G.; Kim, K. A Roadmap for Graphene. *Nature* **2012**, *490*, 192–200.
- Li, X.; Cai, W.; An, J.; Kim, S.; Nah, J.; Yang, D.; Piner, R.; Velamakanni, A.; Jung, I.; Tutuc, E.; *et al.* Large-Area Synthesis of High-Quality and Uniform Graphene Films on Copper Foils. *Science* **2009**, *324*, 1312–1314.
- Bae, S.; Kim, H.; Lee, Y.; Xu, X.; Park, J.-S.; Zheng, Y.; Balakrishnan, J.; Lei, T.; Ri Kim, H.; Song, Y., II; *et al.* Roll-to-Roll Production of 30-Inch Graphene Films for Transparent Electrodes. *Nat. Nanotechnol.* **2010**, *5*, 574–578.
- Hofmann, S.; Sharma, R.; Ducati, C.; Du, G.; Mattevi, C.; Cepek, C.; Cantoro, M.; Pisana, S.; Parvez, A.; Cervantes-Sodi, F.; *et al.* *In Situ* Observations of Catalyst Dynamics During Surface-Bound Carbon Nanotube Nucleation. *Nano Lett.* **2007**, *7*, 602–608.
- Weatherup, R. S.; Bayer, B. C.; Blume, R.; Ducati, C.; Baehtz, C.; Schlögl, R.; Hofmann, S. *In Situ* Characterization of Alloy Catalysts for Low-Temperature Graphene Growth. *Nano Lett.* **2011**, *11*, 4154–4160.
- Yu, Q.; Lian, J.; Siriponglert, S.; Li, H.; Chen, Y. P.; Pei, S. S. Graphene Segregated on Ni Surfaces and Transferred to Insulators. *Appl. Phys. Lett.* **2008**, *93*, 113103.
- Reina, A.; Thiele, S.; Jia, X.; Bhaviripudi, S.; Dresselhaus, M. S.; Schaefer, J. A.; Kong, J. Growth of Large-Area Single- and Bi-Layer Graphene by Controlled Carbon Precipitation on Polycrystalline Ni Surfaces. *Nano Res.* **2009**, *9*, 30–35.
- Shelton, J.; Patil, H.; Blakely, J. Equilibrium Segregation of Carbon to a Nickel (111) Surface: A Surface Phase Transition. *Surf. Sci.* **1974**, *43*, 493–520.
- Oshima, C.; Nagashima, A. Ultra-Thin Epitaxial Films of Graphite and Hexagonal Boron Nitride on Solid Surfaces. *J. Phys.: Condens. Matter* **1997**, *9*, 1–20.
- Grüneis, A.; Kummer, K.; Vyalikh, D. V. Dynamics of Graphene Growth on a Metal Surface: A Time-Dependent Photoemission Study. *New J. Phys.* **2009**, *11*, 073050.
- Weatherup, R.; Dlubak, B.; Hofmann, S. Kinetic Control of Catalytic CVD for High Quality Graphene at Low Temperatures. *ACS Nano* **2012**, *6*, 9996–10003.
- Kidambi, P. R.; Ducati, C.; Dlubak, B.; Gardiner, D.; Weatherup, R. S.; Martin, M.-B.; Senéor, P.; Coles, H.; Hofmann, S. The Parameter Space of Graphene Chemical Vapor Deposition

- on Polycrystalline Cu. *J. Phys. Chem. C* **2012**, *116*, 22492–22501.
13. Li, X.; Cai, W.; Colombo, L.; Ruoff, R. S. Evolution of Graphene Growth on Ni and Cu by Carbon Isotope Labeling. *Nano Lett.* **2009**, *9*, 4268–4272.
 14. Klink, C.; Stensgaard, I.; Besenbacher, F.; Lægsgaard, E. An STM Study of Carbon-Induced Structures on Ni(111): Evidence for a Carbide-Phase Clock Reconstruction. *Surf. Sci.* **1995**, *342*, 250–260.
 15. Lahiri, J.; Miller, T.; Adamska, L.; Oleynik, I. I.; Batzill, M. Graphene Growth on Ni(111) by Transformation of a Surface Carbide. *Nano Lett.* **2011**, *11*, 518–22.
 16. Odahara, G.; Otani, S.; Oshima, C.; Suzuki, M.; Yasue, T.; Koshikawa, T. *In Situ* Observation of Graphene Growth on Ni(111). *Surf. Sci.* **2011**, *605*, 1095–1098.
 17. Lahiri, J.; S. Miller, T.; J. Ross, A.; Adamska, L.; Oleynik, I. I.; Batzill, M. Graphene Growth and Stability at Nickel Surfaces. *New J. Phys.* **2011**, *13*, 025001.
 18. Addou, R.; Dahal, A.; Sutter, P.; Batzill, M. Monolayer Graphene Growth on Ni(111) by Low Temperature Chemical Vapor Deposition. *Appl. Phys. Lett.* **2012**, *100*, 021601.
 19. Jacobson, P.; Stöger, B.; Garhofer, A.; Parkinson, G. S.; Schmid, M.; Caudillo, R.; Mittendorfer, F.; Redinger, J.; Diebold, U. Nickel Carbide as a Source of Grain Rotation in Epitaxial Graphene. *ACS Nano* **2012**, *6*, 3564–72.
 20. Dahal, A.; Addou, R.; Sutter, P.; Batzill, M. Graphene Monolayer Rotation on Ni(111) Facilitates Bilayer Graphene Growth. *Appl. Phys. Lett.* **2012**, *100*, 241602.
 21. Weatherup, R. S.; Bayer, B. C.; Blume, R.; Baehtz, C.; Kidambi, P. R.; Fouquet, M.; Wirth, C. T.; Schlögl, R.; Hofmann, S. On the Mechanisms of Ni-Catalysed Graphene Chemical Vapor Deposition. *ChemPhysChem* **2012**, *13*, 2544–2549.
 22. Hofmann, S.; Blume, R.; Wirth, C. T.; Cantoro, M.; Sharma, R.; Ducati, C.; Hävecker, M.; Zafeiratos, S.; Schnoerch, P.; Oestereich, A.; *et al.* State of Transition Metal Catalysts during Carbon Nanotube Growth. *J. Phys. Chem. C* **2009**, *113*, 1648–1656.
 23. Wirth, C. T.; Bayer, B. C.; Gamalski, A. D.; Esconjauregui, S.; Weatherup, R. S.; Ducati, C.; Baehtz, C.; Robertson, J.; Hofmann, S. The Phase of Iron Catalyst Nanoparticles during Carbon Nanotube Growth. *Chem. Mater.* **2012**, *24*, 4633–4640.
 24. Dong, G. C.; van Baarle, D. W.; Rost, M. J.; Frenken, J. W. M. Graphene Formation on Metal Surfaces Investigated by *in Situ* Scanning Tunneling Microscopy. *New J. Phys.* **2012**, *14*, 053033.
 25. Ehrlich, G. Direct Observations of the Surface Diffusion of Atoms and Clusters. *Surf. Sci.* **1991**, *246*, 1–12.
 26. Jacobson, P.; Stöger, B.; Garhofer, A.; Parkinson, G. S.; Schmid, M.; Caudillo, R.; Mittendorfer, F.; Redinger, J.; Diebold, U. Disorder and Defect Healing in Graphene on Ni(111). *J. Phys. Chem. Lett.* **2011**, *3*, 136–139.
 27. Zhao, W.; Kozlov, S. M.; Höfert, O.; Gotterbarm, K.; Lorenz, M. P. A.; Viñes, F.; Papp, C.; Görling, A.; Steinrück, H.-P. Graphene on Ni(111): Coexistence of Different Surface Structures. *J. Phys. Chem. Lett.* **2011**, *2*, 759–764.
 28. Dzemiantsova, L. V.; Karolak, M.; Lofink, F.; Kubetzka, A.; Sachs, B.; von Bergmann, K.; Hankemeier, S.; Wehling, T. O.; Frömter, R.; Oepen, H. P.; *et al.* Multiscale Magnetic Study of Ni(111) and Graphene on Ni(111). *Phys. Rev. B* **2011**, *84*, 205431.
 29. Karpan, V. M.; Khomyakov, P. A.; Starikov, A. A.; Giovannetti, G.; Zwierzycki, M.; Talanana, M.; Brocks, G.; van den Brink, J.; Kelly, P. J. Theoretical Prediction of Perfect Spin Filtering at Interfaces between Close-Packed Surfaces of Ni or Co and Graphite or Graphene. *Phys. Rev. B* **2008**, *78*, 195419.
 30. Vang, R. T.; Honkala, K.; Dahl, S.; Vestergaard, E. K.; Schnadt, J.; Lægsgaard, E.; Clausen, B. S.; Nørskov, J. K.; Besenbacher, F. Ethylene Dissociation on Flat and Stepped Ni(111): A Combined STM and DFT Study. *Surf. Sci.* **2006**, *600*, 66–77.
 31. Morar, J.; Himpfel, F.; Hollinger, G. C1s Excitation Studies of Diamond (111). I. Surface Core Levels. *Phys. Rev. B* **1986**, *33*, 1340–1345.
 32. Webb, M. J.; Palmgren, P.; Pal, P.; Karis, O.; Grennberg, H. A Simple Method To Produce Almost Perfect Graphene on Highly Oriented Pyrolytic Graphite. *Carbon* **2011**, *49*, 3242–3249.
 33. Lander, J. J.; Kern, H. E.; Beach, A. L. Solubility and Diffusion Coefficient of Carbon in Nickel: Reaction Rates of Nickel-Carbon Alloys with Barium Oxide. *J. Appl. Phys.* **1952**, *23*, 1305–1309.
 34. Díaz, J.; Paolicelli, G.; Ferrer, S.; Comin, F. Separation of the sp³ and sp² Components in the C1s Photoemission Spectra of Amorphous Carbon Films. *Phys. Rev. B* **1996**, *54*, 8064–8069.
 35. Varykhalov, A.; Sánchez-Barriga, J.; Shikin, A.; Biswas, C.; Vescovo, E.; Rybkin, A.; Marchenko, D.; Rader, O. Electronic and Magnetic Properties of Quasifreestanding Graphene on Ni. *Phys. Rev. Lett.* **2008**, *101*, 157601.
 36. Tanaka, K.; Hirano, H. Isolation of Intermediate Compounds of Catalytic Reactions on Single Crystal Surfaces. *Catal. Lett.* **1992**, *12*, 1–6.
 37. Stierle, A.; Molenbroek, A. Novel *in Situ* Probes for Nanocatalysis. *MRS Bull.* **2007**, *32*, 1001–1009.
 38. Kozlov, S.; Viñes, F.; Görling, A. Bonding Mechanisms of Graphene on Metal Surfaces. *J. Phys. Chem. C* **2012**, *116*, 7360–7366.
 39. Starodub, E.; Maier, S.; Stass, I.; Bartelt, N. C.; Feibelman, P. J.; Salmeron, M.; McCarty, K. F. Graphene Growth by Metal Etching on Ru(0001). *Phys. Rev. B* **2009**, *80*, 235422.
 40. Günther, S.; Dänhardt, S.; Wang, B.; Bocquet, M.-L.; Schmitt, S.; Winterlin, J. Single Terrace Growth of Graphene on a Metal Surface. *Nano Lett.* **2011**, *11*, 1895–1900.
 41. Arnoult, W.; McLellan, R. The Solubility of Carbon in Rhodium, Ruthenium, Iridium and Rhenium. *Scr. Metall. Mater.* **1972**, *6*, 1013–1018.
 42. Lacovig, P.; Pozzo, M.; Alfè, D.; Vilmercati, P.; Baraldi, A.; Lizzit, S. Growth of Dome-Shaped Carbon Nanoislands on Ir(111): The Intermediate Between Carbide Clusters and Quasi-Free-Standing Graphene. *Phys. Rev. Lett.* **2009**, *103*, 166101.
 43. Miniussi, E.; Pozzo, M.; Baraldi, A.; Vesselli, E.; Zhan, R. R.; Comelli, G.; Menteş, T. O.; Niño, M. A.; Locatelli, A.; Lizzit, S.; *et al.* Thermal Stability of Corrugated Epitaxial Graphene Grown on Re(0001). *Phys. Rev. Lett.* **2011**, *106*, 216101.
 44. Mittendorfer, F.; Garhofer, A.; Redinger, J.; Klimeš, J.; Harl, J.; Kresse, G. Graphene on Ni(111): Strong Interaction and Weak Adsorption. *Phys. Rev. B* **2011**, *84*, 201401.
 45. Helveg, S.; López-Cartes, C.; Sehested, J.; Hansen, P. L.; Clausen, B. S.; Rostrup-Nielsen, J. R.; Abild-Pedersen, F.; Nørskov, J. K. Atomic-Scale Imaging of Carbon Nanofiber Growth. *Nature* **2004**, *427*, 426–429.
 46. Zhang, Y.; Gao, T.; Xie, S.; Dai, B.; Fu, L.; Gao, Y.; Chen, Y.; Liu, M.; Liu, Z. Different Growth Behaviors of Ambient Pressure Chemical Vapor Deposition Graphene on Ni(111) and Ni Films: A Scanning Tunneling Microscopy Study. *Nano Res.* **2012**, *5*, 402–411.
 47. Sutter, E.; Albrecht, P.; Sutter, P. Graphene Growth on Polycrystalline Ru Thin Films. *Appl. Phys. Lett.* **2009**, *95*, 133109.
 48. Africh, C.; Esch, F.; Comelli, G.; Rosei, R. Dynamics of the O Induced Reconstruction of the Rh(110) Surface: A Scanning Tunneling Microscopy Study. *J. Chem. Phys.* **2001**, *115*, 477–481.
 49. Bluhm, H.; Hävecker, M.; Knop-Gericke, A.; Kiskinova, M.; Schlögl, R.; Salmeron, M. *In Situ* X-Ray Photoelectron Studies of Gas-Solid Interfaces at Near-Ambient Conditions. *MRS Bull.* **2007**, *32*, 1022–1030.